

---

*This copy is for your personal, non-commercial use only.*

---

**If you wish to distribute this article to others**, you can order high-quality copies for your colleagues, clients, or customers by [clicking here](#).

**Permission to republish or repurpose articles or portions of articles** can be obtained by following the guidelines [here](#).

**The following resources related to this article are available online at [www.sciencemag.org](http://www.sciencemag.org) (this information is current as of October 22, 2011 ):**

A correction has been published for this article at:  
<http://www.sciencemag.org/content/284/5422/1929.4.full.html>

**Updated information and services**, including high-resolution figures, can be found in the online version of this article at:  
<http://www.sciencemag.org/content/284/5419/1495.full.html>

This article **cites 31 articles**, 3 of which can be accessed free:  
<http://www.sciencemag.org/content/284/5419/1495.full.html#ref-list-1>

This article has been **cited by** 348 article(s) on the ISI Web of Science

This article has been **cited by** 20 articles hosted by HighWire Press; see:  
<http://www.sciencemag.org/content/284/5419/1495.full.html#related-urls>

This article appears in the following **subject collections**:  
Planetary Science  
[http://www.sciencemag.org/cgi/collection/planet\\_sci](http://www.sciencemag.org/cgi/collection/planet_sci)

# The Global Topography of Mars and Implications for Surface Evolution

David E. Smith,<sup>1\*</sup> Maria T. Zuber,<sup>1,2</sup> Sean C. Solomon,<sup>3</sup>  
 Roger J. Phillips,<sup>4</sup> James W. Head,<sup>5</sup> James B. Garvin,<sup>1</sup>  
 W. Bruce Banerdt,<sup>6</sup> Duane O. Muhleman,<sup>7</sup> Gordon H. Pettengill,<sup>2</sup>  
 Gregory A. Neumann,<sup>1,2</sup> Frank G. Lemoine,<sup>1</sup> James B. Abshire,<sup>1</sup>  
 Oded Aharonson,<sup>2</sup> C. David Brown,<sup>4</sup> Steven A. Hauck,<sup>4</sup>  
 Anton B. Ivanov,<sup>7</sup> Patrick J. McGovern,<sup>3</sup> H. Jay Zwally,<sup>1</sup>  
 Thomas C. Duxbury<sup>6</sup>

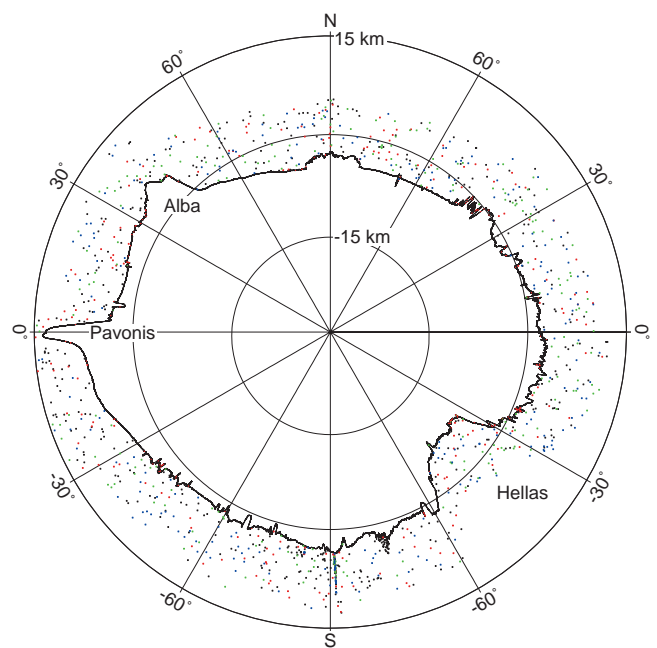
Elevations measured by the Mars Orbiter Laser Altimeter have yielded a high-accuracy global map of the topography of Mars. Dominant features include the low northern hemisphere, the Tharsis province, and the Hellas impact basin. The northern hemisphere depression is primarily a long-wavelength effect that has been shaped by an internal mechanism. The topography of Tharsis consists of two broad rises. Material excavated from Hellas contributes to the high elevation of the southern hemisphere and to the scarp along the hemispheric boundary. The present topography has three major drainage centers, with the northern lowlands being the largest. The two polar cap volumes yield an upper limit of the present surface water inventory of 3.2 to 4.7 million cubic kilometers.

Long-wavelength topography (changes in topography over scales of hundreds to thousands of kilometers) reflects processes that have shaped Mars on a global scale and thus is of particular interest in the context of the planet's evolution. The Mars Orbiter Laser Altimeter (MOLA) (1), an instrument on the Mars Global Surveyor (MGS) spacecraft (2), recently acquired the first globally distributed, high-resolution measurements of the topography of Mars (3). A geodetically controlled topographic model derived from circum-Mars (Fig. 1) and northern hemisphere (4, 5) profiles has enabled quantitative characterization of global-scale processes that have shaped the martian surface.

Before the MGS mission, models of martian topography were derived from Earth-based radar ranging (6), Mariner 9 and Viking 1 and 2 radio occultations (7), stereo and photoclinometric observations from Mariner

9 and Viking imagery (8), and the Mariner 9 ultraviolet and infrared spectrometers (9). Disparate measurement types were combined into digital terrain models (10) that were of variable spatial resolution and typically characterized by vertical errors of ~1 to 3 km. The model from MOLA (Fig. 2) (11) has a spatial resolution of ~1° (or ~59 km separation at the equator) and an absolute accuracy of 13 m with respect to Mars' center of

**Fig. 1.** Global profile of Mars from MOLA crossing longitudes 52°E and 247°E. The north and south polar caps are at the top and bottom. The Pavonis Mons and Alba Patera volcanic shields, both located within the Tharsis province, appear at the upper left, and the Hellas impact basin is at the lower right. The contrast in elevation and regional topographic roughness between the northern and southern hemispheres is also apparent. The dichotomy boundary scarp can be seen at ~50° east of north. Distributed points above the surface correspond to false returns caused by solar background at the laser wavelength and represent <0.5% of the transmitted pulses. Clustered returns above the surface near the south pole are from clouds. The vertical exaggeration is 100:1.



mass (COM) (12). The global topography of Mars is now known to greater accuracy than Earth's continents in a root mean square (rms) sense.

**Global shape.** The difference of ~20 km between the polar and equatorial radii indicates that the largest contribution to shape is the planetary flattening (Table 1), which is due mostly to the rotation of Mars with a small contribution (~5%) (13) from the vast volcano-tectonic Tharsis province (Fig. 2), situated near the equator. Subtraction of the gravitational potential or geoid (14) from radii measurements represents elevations in terms of topography and eliminates the contribution due to rotation, thus clarifying other long-wavelength components of the shape. Figure 2 illustrates that topography on Mars has a 30-km dynamic range, the largest of the terrestrial planets. The large topographic excursions are due to ancient impact basins, large shield volcanoes, and the ability of the planet's rigid outer shell (lithosphere) to support significant stresses associated with surface and subsurface loads (15).

A useful representation of the planetary shape is the triaxial ellipsoid, for which the axes and orientation with respect to a coordinate system with origin at the COM of Mars are given in Table 1. The best fit ellipsoid (16) is dominated by a displacement from the COM by -2986 m along the *z* axis, which represents an offset between the COM and the planet's geometric center or center of figure (COF) along the polar axis. The sign of the offset indicates that the south pole has a higher elevation than the north pole by ~6 km, which corresponds to a systematic south-to-north downward slope of 0.036°. The tri-

<sup>1</sup>Earth Sciences Directorate, NASA/Goddard Space Flight Center, Greenbelt, MD 20771, USA. <sup>2</sup>Department of Earth, Atmospheric, and Planetary Sciences, Massachusetts Institute of Technology, Cambridge, MA 02139, USA. <sup>3</sup>Department of Terrestrial Magnetism, Carnegie Institution of Washington, Washington, DC 20015, USA. <sup>4</sup>Department of Earth and Planetary Sciences, Washington University, St. Louis, MO 63130, USA. <sup>5</sup>Department of Geological Sciences, Brown University, Providence, RI 02912, USA. <sup>6</sup>Jet Propulsion Laboratory, Pasadena, CA 91109, USA. <sup>7</sup>Division of Geological and Planetary Sciences, California Institute of Technology, Pasadena, CA 91125, USA.

\*To whom correspondence should be addressed. E-mail: dsmith@tharsis.gsfc.nasa.gov

axial ellipsoid is also displaced by  $-1428$  m along the  $y$  axis, in the general direction of the Tharsis topographic rise (Fig. 2).

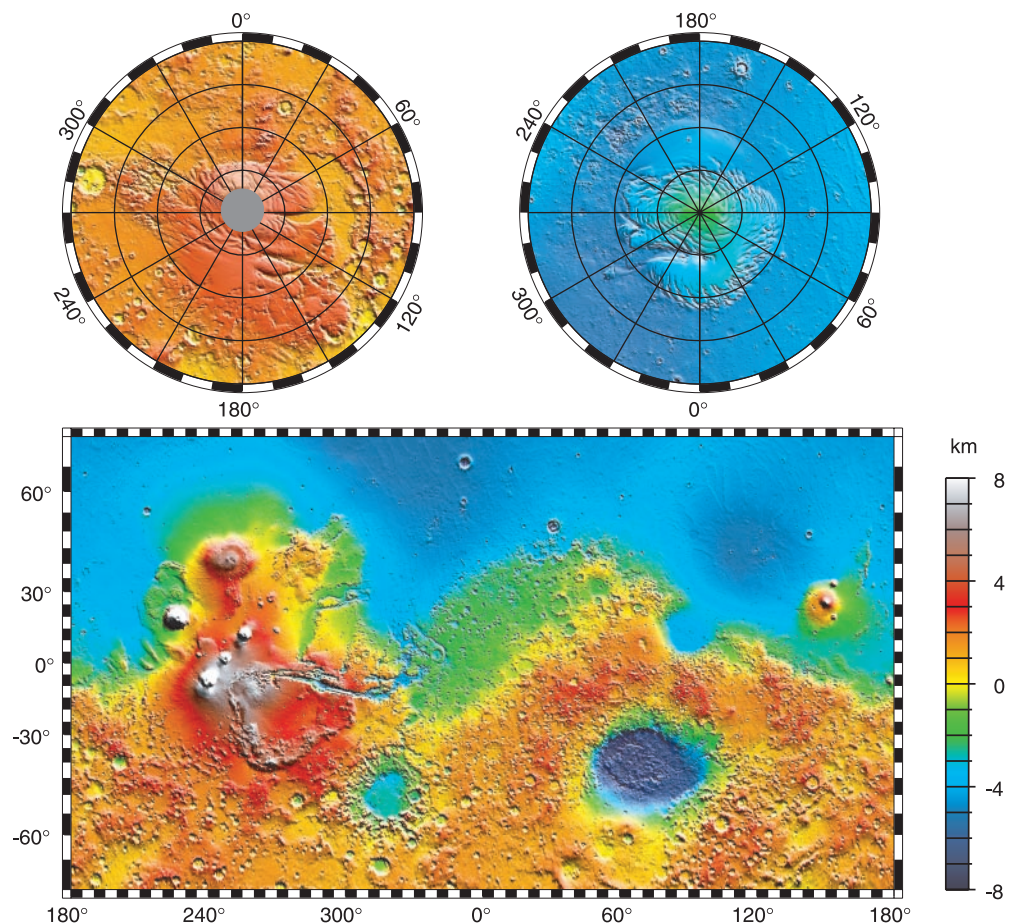
**Major features of topography.** The dominant feature of the topography is the striking difference ( $\sim 5$  km) in elevation between the low northern hemisphere and high southern hemisphere that represents one of the outstanding issues of martian evolution. This hemispheric dichotomy also has a distinctive expression in the surface geology of Mars. The surface of the crust in the southern hemisphere is old and heavily cratered, whereas that in the north is younger and more lightly cratered and was probably volcanically resurfaced early in Mars' history (17). The hemispheric difference is also manifest in surface roughness (Fig. 3) calculated from the MOLA topographic profile data (18). Most of the northern lowlands is composed of the Late Hesperian-aged (19) Vastitas Borealis Formation, which is flat and smooth (Fig. 2), even at a scale as short as 300 m (Fig. 3). The Amazonian-aged (19) Arcadia Formation, which overlies the Vastitas Borealis Formation, is also smooth at large and small scales, consistent with either a sedimentary (4, 20) or volcanic (21) origin for these plains. In the southern hemisphere Noachian-aged (19) ridged plains form locally flat intercrater deposits, whereas younger Hesperian-aged ridged plains dominate in some regions. All are characterized by a rougher topography than the northern plains. The boundary between the smooth northern hemisphere and the rough southern hemisphere is characterized by mesas, knobs, and intervening plains (22), as well as regional elevation changes of up to 4 km over distances of 300 to 1300 km (23). Where the regional elevation change is relatively steep, it is referred to as the dichotomy boundary scarp (compare Fig. 1).

The Tharsis province is a vast region of volcanism and deformation that appears to interrupt the global dichotomy boundary between the southern cratered highlands and northern lowland plains (24). In previous work the province was displayed as a broad topographic rise (10). However, Fig. 2 (see also Fig. 6) shows that topographically Tharsis actually consists of two broad rises. The larger southern rise is superposed on the highlands as a quasi-circular feature that extends from  $\sim 220^\circ\text{E}$  to  $\sim 300^\circ\text{E}$  and from  $\sim 50^\circ\text{S}$  to  $\sim 20^\circ\text{N}$  and spans about  $10^7$  km<sup>2</sup> in area. The highest portion of the southern rise contains the Tharsis Montes (Ascraeus, Pavonis, and Arsia). Eastward of the highest terrain but still elevated are the ridged plains of Lunae Planum (Fig. 2). The smaller northern rise is superposed on the lowlands and covers

approximately the same longitude band as the southern rise, but extends to  $\sim 60^\circ\text{N}$ . The northern rise is dominated by the massive volcanic construct of Alba Patera (compare Fig. 1). Hesperian-aged volcanic fans emanate radially from this shield into the northern lowlands for distances of more than 1000 km. The new data emphasize the distinctive nature of the Alba Patera structure as well as its connection to the Tharsis Montes region. In contrast, the massive Olympus Mons volcano appears to sit off the western edge of the Tharsis rise rather than on the flank, as previously mapped (10). By its spatial association, Olympus Mons is nonetheless likely to have had a genetic link to volcanism in Tharsis proper.

The new topographic data illuminate a long-standing debate over the dominant contributors to the high elevations of the Tharsis region. A prominent ridge (containing Claritas Fossae; Fig. 2) extends southward from the region of the Tharsis Montes, and then curves northeastward in a "scorpion tail" pattern. This arcuate ridge bounds Solis Planum, a plateau within the southern rise. The ridge contains an abundance of heavily cratered Noachian material that has presumably escaped resurfacing by younger Tharsis volcanic flows because of its high elevation. It has been suggested (25) that the termination of

**Fig. 2.** Maps of the global topography of Mars. The projections are Mercator to  $70^\circ$  latitude and stereographic at the poles with the south pole at left and north pole at right. Note the elevation difference between the northern and southern hemispheres. The Tharsis volcano-tectonic province is centered near the equator in the longitude range  $220^\circ\text{E}$  to  $300^\circ\text{E}$  and contains the vast east-west trending Valles Marineris canyon system and several major volcanic shields including Olympus Mons ( $18^\circ\text{N}$ ,  $225^\circ\text{E}$ ), Alba Patera ( $42^\circ\text{N}$ ,  $252^\circ\text{E}$ ), Ascraeus Mons ( $12^\circ\text{N}$ ,  $248^\circ\text{E}$ ), Pavonis Mons ( $0^\circ$ ,  $247^\circ\text{E}$ ), and Arsia Mons ( $9^\circ\text{S}$ ,  $239^\circ\text{E}$ ). Regions and structures discussed in the text include Solis Planum ( $25^\circ\text{S}$ ,  $270^\circ\text{E}$ ), Lunae Planum ( $10^\circ\text{N}$ ,  $290^\circ\text{E}$ ), and Claritas Fossae ( $30^\circ\text{S}$ ,  $255^\circ\text{E}$ ). Major impact basins include Hellas ( $45^\circ\text{S}$ ,  $70^\circ\text{E}$ ), Argyre ( $50^\circ\text{S}$ ,  $320^\circ\text{E}$ ), Isidis ( $12^\circ\text{N}$ ,  $88^\circ\text{E}$ ), and Utopia ( $45^\circ\text{N}$ ,  $110^\circ\text{E}$ ). This analysis uses an areocentric coordinate convention with east longitude positive. Note that color scale saturates at elevations above 8 km.



RESEARCH ARTICLES

the ridge structure could have formed by lithospheric buckling, as could, by analogy, other ridge structures in the south Tharsis region. The southern rise (southward of ~35°S) also contains exposures of heavily cratered Noachian units. These elevated ancient terrains are consistent with the view that the broad expanse of the southern rise (elevations >~3 km; see Fig. 2) formed at least in part by structural uplift (26). Such a hypothesis is supported by the orientation of fractures and graben in Claritas Fossae (24), although it is also possible that there has been a contribution from lateral tectonic forces (25). The high elevations of the Tharsis Montes region as well as of the northern rise display major contributions from volcanic construction (27), although some structural uplift may have subsequently been masked by volcanism (28).

The Hellas impact basin has the deepest topography on Mars and is characterized by a total relief of more than 9 km (Fig. 4). Mountains and massifs previously identified as constituting the main basin ring of Hellas have a diameter of ~2300 km (29) and are situated on the inner slopes of the topographic basin (Fig. 4). Basin ejecta material surrounding Hellas has not been mapped at the global scale; units that surround the basin are dominated by Noachian-aged heavily cratered plains (19). MOLA data reveal, however, a peak in the distinctive topographic annulus that surrounds Hellas at a diameter of ~4000 km, lying ~2 km above the main ring.

In terms of size and morphology, Hellas has striking similarities to the South Pole-Aitken basin on the farside of the moon. These two impact structures have similar diameters and volumes (30), as well as distributions of surrounding excavated material, though the material encircling South Pole-Aitken is more asymmetric. Hellas represents a major topographic excursion that dominates much of Mars' southern hemisphere topography (compare Fig. 1). Previous researchers have noted the great depression, but no previous topographic model has resolved the expanse of Hellas' exterior topographic annulus, which is likely due to ejecta, but possibly includes contributions from impact melt, structural uplift, and admixed local material. This material represents a major redistribution of Mars' early crust. Figure 4 was used to determine that the volume of the topographic annulus, if "refilled" into the basin, would cause the basin and surroundings to have an elevation of ~600 m with respect to the global reference. Material removed from Hellas thus accounts for a significant amount of the high-standing topography of Mars' southern hemisphere. The observed topographic annulus around Hellas is close to the position of the outermost mapped basin ring [diameter ~4200 km

(29)]. An alternative explanation for the topography is that this outermost ring might represent the highly degraded main basin rim, with additional ring structures lying lower within the basin. Figure 4 also shows that material from Hellas' topographic annulus

contributes to the topographic expression along part of the dichotomy boundary.

**Implications for evolution.** The hemispheric dichotomy represents both an elevation difference and a difference in surface geology, and although these two defining

Table 1. Mars geodetic parameters from MOLA.

Parameter	Value	Uncertainty
Mean radius* (m)	3,389,508	± 3
Mean equatorial radius† (m)	3,396,200	± 160
North polar radius* (m)	3,376,189	± 50
South polar radius* (m)	3,382,580	± 50
Triaxial ellipsoid		
a (m)	3,398,627	
b (m)	3,393,760	
c (m)	3,376,200	
1/flattening	169.8	± 1.0
Directions of principal ellipsoid axes		
a	1.0°N, 72.4°E	
b	0°N, 342.4°E	
c	89.0°N, 252.4°E	
Ellipsoid offset of COF from COM		
Δx (m)	-233	
Δy (m)	-1,428	
Δz (m)	-2,986	
Volume of north polar cap (10 <sup>6</sup> km <sup>3</sup> )‡	1.2 to 1.7	
Volume of south polar cap (10 <sup>6</sup> km <sup>3</sup> )	2 to 3	
Elevation comparison with landers		
Viking 1 (m)	45	
Viking 2 (m)	0	
Pathfinder (m)	94	

\*See (65). †See (66). ‡See (51).

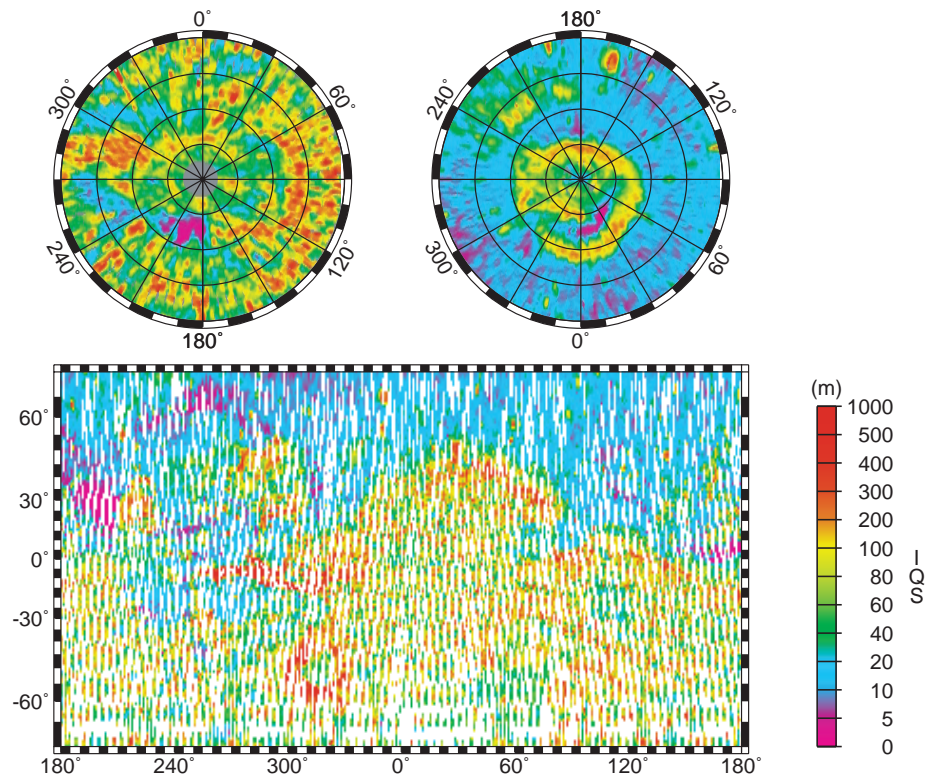


Fig. 3. Interquartile scale (IQS) surface roughness (18) of Mars calculated from MOLA profiles on a 330-m baseline in a 100-km running window. The projections are the same as in Fig. 2.

aspects may be related, they do not necessarily share the same mechanism of formation. Hypotheses to explain the hemispheric dichotomy have included thinning of the northern hemisphere crust by mantle convection (31, 32), an early period of tectonic plate recycling (33), and one or more large impacts in the northern hemisphere (34–36).

A key issue is to determine how much of the hemispheric elevation difference is due to the long-wavelength planetary shape rather than the boundary scarp (23, 37); this issue can be explored from the global distribution of elevations and slopes (Fig. 5). As shown in Fig. 5, which plots histograms of elevations before and after removing the offset between the COM and COF along the polar axis, the *z* component of the COM-COF difference is largely equivalent to the hemispheric elevation difference. A histogram of the distribution of 100-km baseline slopes (38) calculated from the global topographic grid (Fig. 5C) peaks at  $\sim 0.3^\circ$  and is long-tailed, the latter feature a result of topographic excursions associated with volcanoes, impact basins, and tectonic features. The slope corresponding to the peak in the distribution is close to the average longitudinal slope associated with the COM-COF offset along the *z* axis and is partly a result of the offset. But the peak slope also contains contributions due to Tharsis and regional-scale features.

Subtracting the COM-COF offset along the polar axis from the global topography model (Fig. 6) eliminates most of the hemispheric

elevation difference, causing a large part of the southern hemisphere, away from Tharsis and Hellas, to display elevations as low as those over a significant fraction of the northern hemisphere. Together, Figs. 5 and 6 demonstrate that the COM-COF offset accounts for most of the elevation difference between the northern and southern hemispheres and indicate that the hemispheric elevation difference is primarily a long-wavelength effect.

A projection of the northern hemisphere topography from the pole to the equator (Fig. 7) further illustrates the nature of the northern hemisphere depression. Note the distinctive circular signature of the buried Utopia basin, originally proposed as an impact feature on the basis of geological evidence (35), but not observed in earlier topographic studies. The circular expression of Utopia is apparent despite its location within the area of northern hemisphere resurfacing (5, 39). However, even after accounting for the formation of the Tharsis rise, presumably subsequent to the process that produced the hemispheric elevation difference, the boundary of the northern hemisphere depression is clearly noncircular, and we see no compelling topographic evidence for a hemispheric-scale single impact such as previously proposed (34). Formation of the elevation difference by multiple smaller impacts has also been suggested (36). Beyond Utopia, however, no circular structures of comparable scale are apparent in the topography of the northern plains, although arguably such structures could have been

masked by processes that occurred subsequent to formation.

MGS gravity data (40) provide additional perspective on crustal structure beneath the resurfaced northern hemisphere. Large (though smaller than hemispheric-scale) impacts such as Utopia and Hellas are marked by distinctive positive gravitational anomalies (40). However, no other anomalies of comparable spatial scale occur in association with regional topographic lows in the northern hemisphere, except for the previously known Isidis impact structure that sits on the dichotomy boundary. We thus suggest that the long-wavelength topographic expression of the northern hemisphere depression was shaped by an internal process or processes.

**Fig. 4.** Regional topographic model of the Hellas basin. (Top) Azimuthally averaged radial topography used in the calculation of infilling the basin with surrounding material postulated to have been excavated from it. (Bottom) Color-coded topography plotted in an equal-area projection with the same scale as that in Fig. 2. The black lines correspond to zero-elevation contours.

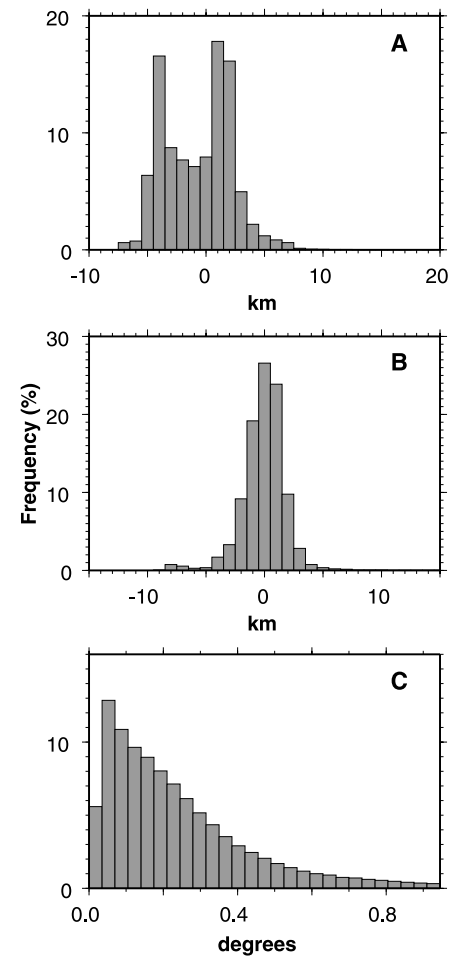
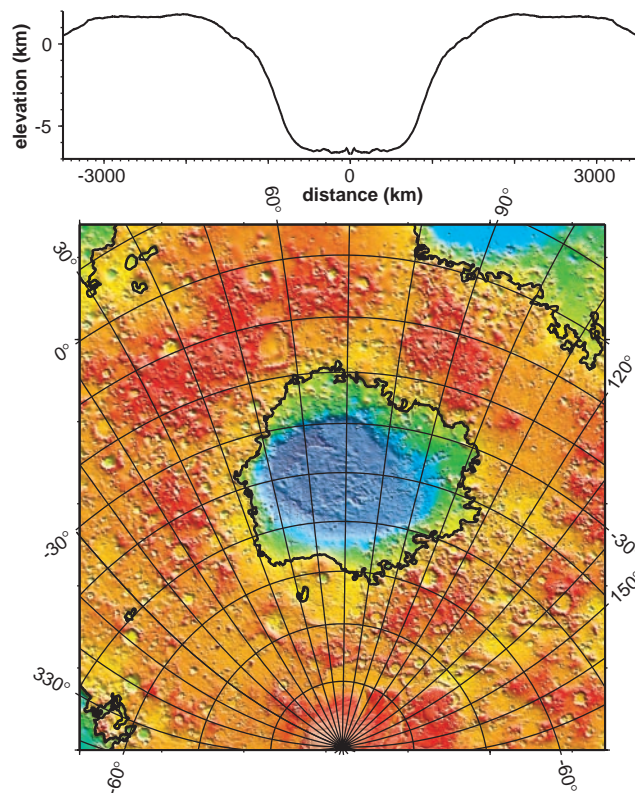


**Fig. 5.** Histograms of (A) topography, (B) heights with respect to an ellipsoid shifted by  $-2.986$  km along the *z* axis, and (C) 100-km baseline slopes. The histogram in (A) shows the distinct bimodal signature that represents the elevation difference between the northern and southern hemispheres. That in (B) shows elevations plotted with respect to an ellipsoid whose center is shifted so as to remove the effect of the COM-COF offset along the polar axis. The effect of the shift is to produce a unimodal distribution of elevations; that is, the hemispheric difference in elevation largely disappears.

The MOLA topography does not permit us to rule out the possibility of a focusing of internal activity in the vicinity of an early impact (36, 41). However, if this focusing occurred, subsequent reworking of the northern crust by internal processes must have obliterated the record of basin circularity.

Distinguishing between internal mechanisms, mantle flow versus plate recycling, will require further study. Mantle convection calculations show that a deep-mantle phase transition would enable the development of hemispheric-scale (harmonic degree 1) convective instabilities on Mars (42), but additional analysis is required to understand how such a mantle flow scenario, coupled with its lithospheric response, could produce the observed long-wavelength topography. Recent observations by the MGS magnetometer experiment show magnetic anomalies of high magnitude that have been interpreted as evidence of an early, vigorous hydrodynamic dynamo in the martian core (43). The largest magnetic anomalies are confined to the southern highland crust, and because anomalies are generally absent near large southern hemisphere impact basins, a rapid decay in the strength of the dynamo and the global magnetic field in the first ~500 million years of martian history is inferred (43). Either an early Noachian era of plate recycling (33, 43) or vigorous mantle convection would be consistent with an early core dynamo.

Important new constraints on the lithospheric thermal structure and heat flow in the southern hemisphere of Mars come from the high relief (Fig. 4) and gravity signature (40) of the Hellas basin and the amplitudes of the largest crustal magnetic anomalies (43). The 9 km of present relief displayed by Hellas implies that the mechanical lithosphere of Mars at the time of basin formation was at least locally of substantial thickness and long-term strength. The implied stress differences supported by martian lithospheric strength exceed those for the South Pole-Aitken basin on the moon (30) with its lower gravitational attraction, and would be larger still if the proposed ~2 to 3 km thickness of Late Noachian to Amazonian units that blanket the floor of Hellas (44) were removed. If the basin is ~90% isostatically compensated, as suggested from gravity data (40), then a basin relaxation model (45) indicates that the elastic lithosphere thickness at the time of Hellas' formation was ~30 km. The thicknesses of coherently magnetized crustal blocks required to account for the observed magnetic anomalies with magnetizations no greater than for common terrestrial rocks also demand that temperatures were below the Curie temperature of the dominant magnetic minerals to significant depths before the Hellas impact event (43). The amplitudes of the magnetic anomalies yield a comparable elas-

tic lithosphere thickness to that inferred from Hellas, but more detailed modeling of gravity, topography, and magnetics will ultimately be required to distinguish whether there existed any resolvable difference in lithospheric thermal structure between the time of Hellas basin formation and earlier.

The proposal that the hemispheric boundary scarp represents a primary structure associated with one or more major impacts (34–36) in the northern hemisphere does not receive strong support from the MOLA data, at least along those portions of the boundary not strongly affected by erosion (22). But the new topographic data do suggest that an impact in the southern hemisphere (Hellas) contributes to the boundary topography in its vicinity. The dichotomy boundary as manifest in surface geology and regional topography appears to contain three dominant contributions: (i) volcanic construction associated with Tharsis, (ii) major excavated deposits approximately circumferential to Hellas, with additional contributions from Isidis and probably Utopia ejecta, and (iii) modification of the intervening region by fluvial processes associated with the outflow channels that empty into Chryse Planitia. In addition, previously documented [for example, (35)] contributions from fracturing and resurfacing dictate that the boundary formed in response to multiple, complex mechanisms.

**Polar caps and present surface volatile budget.** The process that produced the low northern hemisphere occurred early in martian history. The resulting elevation difference must have dominated the transport of water on Mars throughout its history. The

hemispheric elevation contrast also has played a role in the present distribution of surface volatiles, which can be quantified by the MOLA topographic model.

The largest present reservoirs of surface volatiles on Mars are the north and south polar caps (Fig. 2). Visually, the southern ice cap is smaller in extent than the northern, although the southern polar layered deposits extend farther from the ice cap and exhibit a more asymmetric distribution than their northern counterparts (19). Residual ice, which persists throughout the seasonal cycle, is much more limited in extent (an area with about one-third the diameter of the north polar cap) and is offset from the present rotational pole toward 35° to 40°E such that the pole does not fall within the residual ice deposit. The topography is highest in the south polar region within the residual ice deposits (87°S, ~10°E), where a broad dome is present with more than 3 km of relief at one end of the cap (Fig. 8). The relief of the southern polar cap is comparable to that of the northern cap.

The area of probable ice-rich material greatly exceeds the region of residual ice that is apparent from images. Support for this interpretation comes from the existence of distinctive plateau regions that correlate with layered terrain units (19), as would be expected if the layers were deposited on cratered terrain. In addition, impact craters within the plateaus share unusual geometric properties with counterparts in the north polar region (46) that are observed to have formed in an ice-rich substrate. This similarity suggests that significant portions of the south polar ice cap may be buried beneath mantling dust

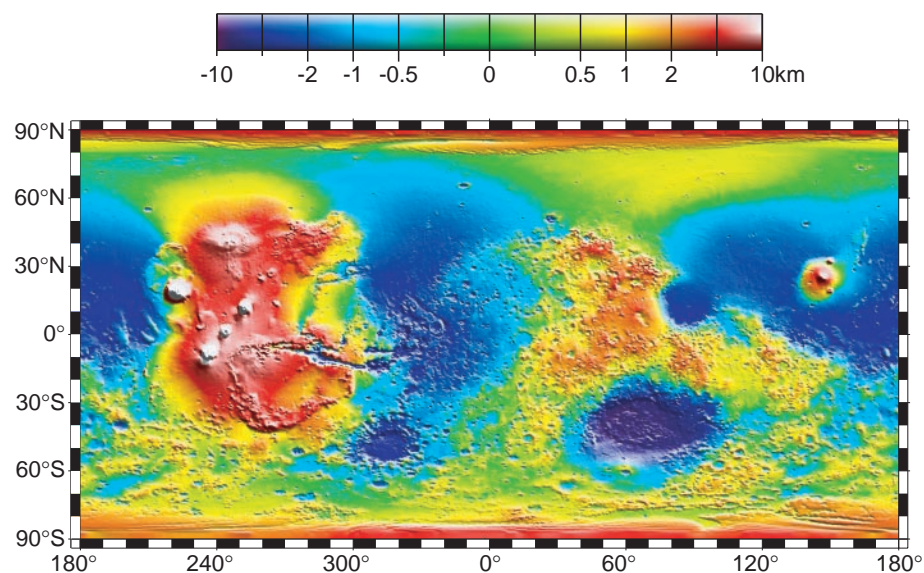


**Fig. 6.** Map of Mars' shape with zonal spherical harmonic degree 1 (COM-COF offset along the polar z axis) removed. The projection is rectangular to show topography from pole to pole. Note the general similarity in elevation between the northern and southern hemispheres. The figure highlights the two other significant components of martian topography: the Tharsis province and the Hellas impact basin. Here we have not removed shorter wavelength topographic features, including those composing the dichotomy boundary scarp.

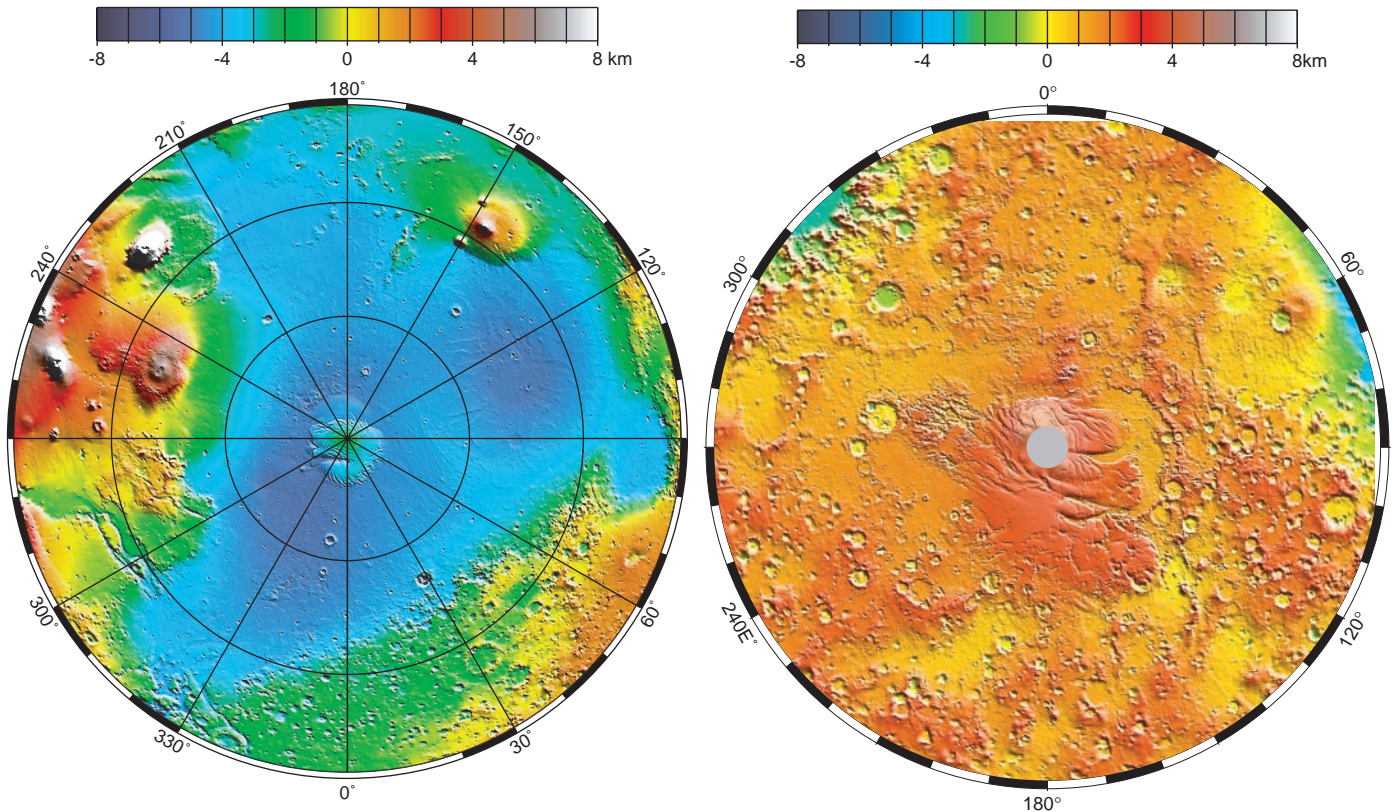


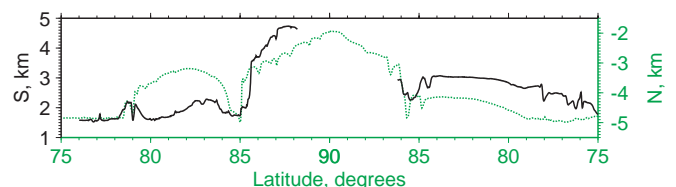
**Fig. 7 (left).** Lambert equal-area projection of pole-to-equator topography in the northern hemisphere. The Utopia basin is the circular depression (in light blue) in the upper right. **Fig. 8 (right).** Polar stereographic projection of topography from latitude 55°S to the pole.

deposits. Third, profiles across the northern and southern caps (Fig. 9) show a striking correspondence in shape that argues for a similarity in composition and suggests that the southern cap may have a significant water ice component. The surface exposure of the residual south polar cap has been observed to display a CO<sub>2</sub> composition (47), which led to the idea that CO<sub>2</sub> is the dominant volatile in the southern cap. However, recent experiments on the rheology of solid CO<sub>2</sub> (48) combined with relative elevation measurements from stereo imaging (49) suggest that H<sub>2</sub>O is the more likely dominant volatile constituent of the southern cap (50), although the dust content in the deposits remains uncertain.

By accounting for the possible contribution of flexure of the basal surface due to the layered deposit load (51, 52), we estimate that the south polar cap has a volume of  $2 \times 10^6$  to  $3 \times 10^6$  km<sup>3</sup>, and that it extends over an area of  $1.44 \times 10^6$  km<sup>2</sup> (53). The average relief above the surroundings is ~815 m. The uncertainty in the volume includes contributions from errors in the mapped surface and the interpolated polar gap, as well as in the depth of the estimated basal surface. The volume of the south polar cap load (ice plus layered deposits) is greater than that calculated for the northern cap (51). But because the thickness of dust that overlies much of the plateau cannot be determined from imaging or thermal inertia data (54), and be-

cause the amount of dust mixed with the ice cannot be distinguished from ice flow models unless the temperature of the ice is known well (55), the volatile content implied by the south polar volume must be considered only an upper limit. The correspondingly greater range of possible densities for the southern layered unit yields potentially larger deflections and flexural infill volumes than the northern cap models (51, 52), thus producing a larger uncertainty in the volume estimation (53). Combined with our previous volume estimate for the northern ice cap (51) (Table 1), we determine a total surface volatile inventory of up to  $3.2 \times 10^6$  to  $4.7 \times 10^6$  km<sup>3</sup>, which is equivalent to a global layer of 22 to 33 m thickness. Even if it is assumed that both caps have a pure H<sub>2</sub>O composition, this range is at the low end of previous estimates of the amount of water believed to have been present early in Mars' history (56). However, the surface water may represent only a fraction of the water believed to be stored currently beneath the surface in the regolith (57).

**Fig. 9.** Comparison of topographic profiles of the southern (solid line) and northern (dotted line) residual ice caps across longitudes 0°E to 180°E. The gaps in the middle of the southern cap profile are due to lack of coverage poleward of 87°S. The northern profile is shifted 6.7 km upward and 1° in latitude, which makes the shapes of the two caps nearly coincident. The vertical exaggeration is 100:1.



Much future work will be needed to reconcile the present surface volatile inventory with primordial estimates and with models of climatic cycling of water and mechanisms of volatile loss.

**Implications for hydrological transport.** The low northern hemisphere has been hypothesized as the site of an early martian ocean (58). One of the proposed “shorelines” corresponds approximately to an equipotential surface, consistent with that hypothesis (20), as is a correlation of low elevation with high topographic smoothness. Application of smoothness data to assess the possible hydrological origin of individual small occurrences of units elsewhere on Mars, however, must be done with caution and in combination with other data [see, for example, (20)]. Smoothness alone can be due to several sources, such as volcanism, as seen in the Amazonian lava flows on the southwestern flanks of Tharsis (Fig. 3).

The MOLA data reveal that there are at

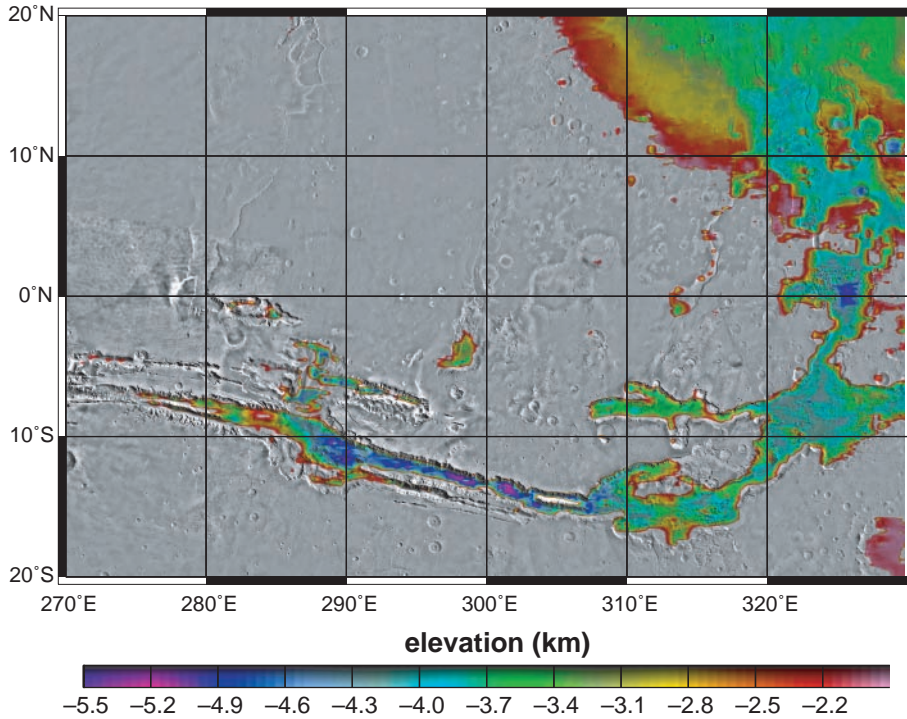


**Fig. 10.** Elevations within the floor of the Valles Marineris canyon system and the adjacent Chryse outflow channels. All areas not color contoured have elevations above  $-1.9$  km.

present, and probably for much of Mars' history, only three major closed basins that can act as sinks for the surficial flow of water or ice (Table 2); the low-lying northern plains are by far the largest of these. Its watershed, the basin along with the remaining area of the planet that would drain into it, constitutes three-quarters of Mars' surface area. The other basins are Hellas and Argyre/Solis Planum, both in the southern hemisphere.

Hellas is much smaller in area than the northern plains, but its great depth gives it a volume that approaches that of the much shallower northern basin. Its floor has the lowest elevation on Mars. The highest closed contour is at 1250 m, at which level it breaches into the Isidis basin. However, Hellas' drainage area is relatively small. Two outflow channels empty into the basin from the east. These likely formed as a result of the interaction of groundwater or ground ice with several ancient southern hemisphere volcanic shields (19). The flat though rough (Fig. 3)

nature of the basin floor can be consistent with fluvial, lacustrine, or aeolian deposition, all of which have been proposed on the basis of geological characterization of the deposits that fill central Hellas (44).

Argyre has a relatively small volume compared with Hellas but has a watershed that is just as large. The watershed breaches into Chryse Planitia through a well-developed set of flood-carved channels. The Solis Planum part of this watershed is unique in comparison with other southern hemisphere drainage centers in that it is apparently a tectonic structure rather than the result of a major impact. The Solis Planum drainage area is very shallow; the mean depth is only  $\sim 500$  m.

The COM-COF offset along the polar axis is responsible for the global-scale south-to-north transport of volatiles indicated by flow directions of outflow channels and valley networks (59), an observation supported by the global distribution of topographic gradients (Fig. 5C). Thus, if surface or near-surface water

on Mars was once ubiquitous, much of it, even at high southern latitudes [such as would be liberated by basal melting (57) of an earlier and significantly thicker south polar cap], would have flowed to the northern plains. If the extended period of formation of the Tharsis province did not significantly modify regional slopes in the southern hemisphere, then Hellas and Argyre would each have collected water from about one-eighth of the planet. Hellas, with its great volume, would have been better able to absorb an influx, whereas Argyre may have breached and drained into the northern basin. Of course, water sources bear closely on the drainage. Recent images (60) indicate that many valley networks formed in response to subsurface sources rather than precipitation. The distribution of subsurface or surface sources would clearly control the water that would have been available to drain into any given area.

Some of the Valles Marineris canyons have been considered as source areas for outflow channels (61). Previous topography (62) was characterized by inconsistent gradients along the canyon floor, but these maps lacked geodetic control. MOLA topography (Fig. 10) now enables accurate calculation of floor slopes and their relation to the adjacent Chryse outflow channels. The canyon system is deepest ( $\sim 11$  km) in Coprates Chasma at  $\sim 300^\circ\text{E}$  where the floor elevation is also lowest in an absolute sense (about  $-5$  km). The increasing trough depths from the head of the canyon to Coprates superimposed on the flank of Tharsis result in a net eastward canyon-floor downward gradient of  $\sim 0.3^\circ$ . East of Coprates, however, the trough floors slope gently uphill by  $\sim 0.03^\circ$ , a gradient that is consistent over at least 1500 km. This uphill slope would present a barrier to surface water flow from Valles Marineris to the chaotic terrain and outflow channels to the northeast unless the water depth was sufficient to overcome the relief difference of  $\sim 1$  km. Local or regional tectonics (for example, rift deepening or large-scale tilting) as well as sediment infilling could explain the east-west floor gradients, and at least some of these processes could have postdated the outflow channels. However, the downhill floor gradient going westward from  $\sim 330^\circ\text{E}$  suggests that certain localized depressions could have served as source areas for water infilling of Valles Marineris.

**Table 2.** Mars global drainage basins.

Region	Highest closed contour (m)	Area ( $10^6$ km $^2$ )	Volume ( $10^6$ km $^3$ )	Watershed ( $10^6$ km $^2$ )
Northern plains*	-2000	50	100	110
Hellas	1250	9	60	20
Argyre				
Basin	0	1.5	4	20
Solis Planum	3250	1.1	0.55	2

\*The dichotomy boundary was chosen for purposes of computing area and volume.

**References and Notes**

1. M. T. Zuber *et al.*, *J. Geophys. Res.* **97**, 7781 (1992).
2. A. A. Albee, F. D. Palluconi, R. E. Arvidson, *Science* **279**, 1671 (1998).
3. The data set includes topographic profiles of the northern hemisphere collected during the capture orbit, aerobraking hiatus orbit, and Science Phasing Orbit phases of the Mars Global Surveyor mission during the period 15 September 1997 to 31 July 1998, and circum-Mars profiles spanning the latitude range  $87^\circ\text{N}$  to  $87^\circ\text{S}$  for the period 1 March to 15 April 1999.
4. D. E. Smith *et al.*, *Science* **279**, 1686 (1998).



## RESEARCH ARTICLES

5. M. T. Zuber *et al.*, *Geophys. Res. Lett.* **25**, 4393 (1998).
6. L. E. Roth, G. S. Downs, R. S. Saunders, G. Schubert, *Icarus* **42**, 287 (1980); G. S. Downs, P. J. Mousinis-Mark, S. H. Zisk, T. W. Thompson, *J. Geophys. Res.* **87**, 9747 (1982).
7. A. J. Kliore, D. L. Cain, G. Fjeldbo, B. L. Seidel, M. J. Sykes, *Icarus* **17**, 484 (1972); G. F. Lindal *et al.*, *J. Geophys. Res.* **84**, 8443 (1979).
8. L. A. Soderblom and D. B. Wenner, *Icarus* **34**, 622 (1978); S. S. C. Wu, P. A. Garcia, R. Jordan, F. J. Schafer, *Nature* **309**, 432 (1984).
9. C. W. Hord, *Icarus* **17**, 443 (1972); B. Conrath *et al.*, *J. Geophys. Res.* **78**, 4267 (1973).
10. S. S. C. Wu, *U.S. Geol. Surv. Map I-2160* (1991).
11. In the current topographic model, which combines elliptical and mapping orbit observations, ground shots with valid spacecraft-attitude knowledge, with pointing angle  $<6^\circ$  except where off-nadir ranging was performed to cover the north pole, numbered 26.6 million. All ground shots were projected sinusoidally and binned on a  $1^\circ$  by  $1^\circ$  equal-area global grid, and the median topography and location coordinates were obtained. Planetary radii were projected and similarly binned. A 36th degree-and-order harmonic model was fit to the data by least squares. This harmonic model was used in the determination of the best-fit ellipsoid.
12. The MOLA instrument measures the round trip time of flight of individual laser pulses between the MGS spacecraft and the martian surface. Each measurement is tagged at the transmit time; the receive time of the pulse is derived from the time of flight and the transmit time. The spacecraft inertial positions are derived for both transmit and receive times, and the light path is traced from the transmit position to the surface (accounting for spacecraft attitude) and back to the spacecraft at the receive position and time. The martian radius is obtained for the coordinates of the "bounce point" of the laser pulse on the surface in a COM reference frame. In the MGS mapping orbit the instrument's 10-Hz sampling rate combined with the laser beam divergence of  $400 \mu\text{rad}$  results in a surface spot size of  $\sim 160$  m and shot-to-shot spacings of  $\sim 330$  m. The precision of MOLA range measurements approaches the limiting resolution of 37.5 cm on smooth level surfaces and may increase up to  $\sim 10$  m on  $30^\circ$  slopes. The accuracy of the spot location in latitude and longitude is limited by the knowledge of the spacecraft pointing at 1 to 3 mrad (400 to 2000 m on the surface, depending on the spacecraft altitude) and spacecraft position uncertainties of a few hundred meters. The estimate of global topographic accuracy includes contributions from radial orbit error (7 m rms) (63), instrument error (3 m rms), and geoid error ( $\pm 10$  m rms) (40). The accuracy estimate for the shape of the planet is  $\pm 8$  m. A comparison of the binned altimeter data set with the locations of the Viking 1 and 2 and Pathfinder landing sites shows good agreement (Table 1).
13. W. M. Folkner, C. F. Yoder, D. N. Yuan, E. M. Standish, R. A. Preston, *Science* **278**, 1749 (1997); M. T. Zuber and D. E. Smith, *J. Geophys. Res.* **102**, 28673 (1997).
14. This analysis uses the geoid from the MGM8901 gravitational field model of Mars, derived from MGS gravity calibration orbit Doppler tracking, MGS elliptical orbit tracking, and historical tracking data from the Viking 1 and 2 and Mariner 9 orbiters (40). Zero elevation is defined as the equipotential surface whose average value at the equator is equal to 3,396,00 m.
15. D. L. Turcotte, R. J. Willemann, W. F. Haxby, J. Norberry, *J. Geophys. Res.* **86**, 3951 (1981).
16. The best-fit ellipsoid, which includes an estimation of the COM-COF offsets and the directions of the principal axes, has an rms fit of 1.9 km. The new global shape parameters are in close agreement with values obtained in an earlier long-wavelength model based on reanalysis of Viking and Mariner occultation measurements (37).  $x, y, z$  are body-fixed coordinates in a right-handed COM system in which the  $z$  axis is the rotation axis and the  $x$  axis is the origin of longitude.
17. T. A. Mutch, R. E. Arvidson, J. W. Head, K. L. Jones, R. S. Saunders, *The Geology of Mars* (Princeton Univ. Press, Princeton, NJ, 1976); M. H. Carr, *The Surface of Mars* (Yale Univ. Press, New Haven, CT, 1981).
18. Because the topographic distribution function has a long tail as a result of cratering, faulting, and other localized processes, we define regional roughness using the interquartile scale (IQS) variation of topography in a window of width 100 km along individual profile tracks. The IQS, defined by the estimator (64)
 
$$R_q = \frac{N}{2N-1} (Q_3 - Q_1)$$
 where  $Q_i$  is the elevation of the  $i$ th quartile point and  $N$  is the number of points, measures the width of a histogram of the most significant 50% of the elevations. The parameter  $R_q$ , which is commonly divided by 0.673 (the IQS of a normal distribution), is a robust estimator in the sense that it is not sensitive to outliers in as much as half of the population or as little as a quarter.
19. D. H. Scott and K. L. Tanaka, *U.S. Geol. Surv. Misc. Inv. Series Map I-1802-A* (1986); R. Greeley and J. E. Guest, *U.S. Geol. Surv. Misc. Inv. Series Map I-1802-B* (1987); K. L. Tanaka and D. H. Scott, *U.S. Geol. Surv. Misc. Inv. Series Map I-1802-C* (1987). Mars is divided into three primary stratigraphic units. The Noachian system is the oldest and consists of ancient cratered terrain. The Hesperian overlies the Noachian and consists principally of ridged plains materials. The Amazonian system has the youngest relative age and is represented mainly by smooth plains.
20. J. W. Head *et al.*, *Geophys. Res. Lett.* **25**, 4401 (1998).
21. A. McEwen *et al.*, *Lunar Planet. Sci.* **30**, 1829 (1999).
22. R. P. Sharp *et al.*, *J. Geophys. Res.* **76**, 331 (1971). R. P. Sharp, *ibid.* **78**, 4073 (1973).
23. H. Frey, S. E. Sakimoto, J. Roark, *Geophys. Res. Lett.* **25**, 4409 (1998).
24. W. B. Banerdt, M. P. Golombek, K. L. Tanaka, in *Mars*, H. H. Kieffer, B. M. Jakosky, C. W. Snyder, M. S. Matthews, Eds. (Univ. of Arizona Press, Tucson, 1992), pp. 249–297; P. B. Esposito *et al.*, *ibid.*, pp. 209–248.
25. R. A. Schultz and K. L. Tanaka, *J. Geophys. Res.* **99**, 8371 (1994); J. Dohm and K. Tanaka, *Planet. Space Sci.* **47**, 411 (1999).
26. W. B. Banerdt, R. J. Phillips, N. H. Sleep, R. S. Saunders, *J. Geophys. Res.* **87**, 9723 (1982).
27. S. C. Solomon and J. W. Head, *ibid.* **82**, 9755 (1982).
28. R. J. Phillips, N. H. Sleep, W. B. Banerdt, *ibid.* **95**, 5089 (1990).
29. R. A. Schultz and H. V. Frey, *ibid.*, p. 14175.
30. M. T. Zuber, D. E. Smith, G. A. Neumann, F. G. Lemoine, *Science* **266**, 1839 (1994).
31. R. E. Lingenfelter and G. Schubert, *Moon* **7**, 172 (1973); D. U. Wise, M. P. Golombek, G. E. McGill, *Icarus* **35**, 456 (1979); *J. Geophys. Res.* **84**, 7934 (1979).
32. G. E. McGill and A. M. Dimitriou, *J. Geophys. Res.* **95**, 12595 (1990).
33. N. H. Sleep, *ibid.* **99**, 5639 (1994).
34. D. E. Wilhelms and S. W. Squyres, *Nature* **309**, 138 (1984).
35. G. E. McGill, *J. Geophys. Res.* **94**, 2753 (1989).
36. H. V. Frey and R. A. Schultz, *Geophys. Res. Lett.* **15**, 229 (1988).
37. D. E. Smith and M. T. Zuber, *Science* **271**, 184 (1996).
38. Slopes were computed in the direction of maximum gradient on 100-km baselines from a global  $0.25^\circ$  grid, smoothed to 100 km. The histogram uses bins of width  $0.035^\circ$ .
39. H. V. Frey, S. E. Sakimoto, J. H. Roark, *Eos Trans. Am. Geophys. Union* **79**, P72A-03 (1998).
40. D. E. Smith, W. L. Sjogren, G. Balmino, G. L. Tyler, in preparation; M. T. Zuber *et al.*, *Eos Trans. Am. Geophys. Union*, in press.
41. G. E. McGill and S. W. Squyres, *Icarus* **93**, 386 (1991).
42. H. Harder and U. R. Christensen, *Nature* **380**, 507 (1996); H. Harder, *J. Geophys. Res.* **103**, 16775 (1998); D. Breuer, D. A. Yuen, T. Spohn, S. Zhang, *Geophys. Res. Lett.* **25**, 229 (1998).
43. M. H. Acuña *et al.*, *Science* **284**, 790 (1999); J. E. P. Connerney *et al.*, *ibid.*, p. 794.
44. R. Wichman and P. Schultz, *J. Geophys. Res.* **94**, 17333 (1989); J. Kargel and R. Strom, *Geology* **20**, 3 (1992); J. Moore and K. Edgett, *Geophys. Res. Lett.* **20**, 1599 (1993); K. Tanaka and G. Leonard, *J. Geophys. Res.* **100**, 5407 (1995).
45. S. Zhong and M. T. Zuber, in preparation.
46. J. B. Garvin, S. E. H. Sakimoto, J. J. Frawley, C. Schnetzler, in preparation.
47. H. H. Kieffer, *J. Geophys. Res.* **84**, 8263 (1979); D. A. Paige *et al.*, *ibid.* **95**, 1319 (1990).
48. W. B. Durham, S. H. Kirby, L. A. Stern, *Lunar Planet. Sci.* **30**, 2017 (1999).
49. P. M. Schenk and J. M. Moore, in preparation.
50. J. F. Nye, W. B. Durham, P. M. Schenk, J. M. Moore, in preparation.
51. M. T. Zuber *et al.*, *Science* **282**, 2053 (1998).
52. C. L. Johnson *et al.*, in preparation.
53. We developed a high-resolution digital terrain model for the region from  $70^\circ\text{S}$  to  $90^\circ\text{S}$ , with the surface elevation interpolated in the polar gap between  $86^\circ$  and  $90^\circ\text{S}$ . For an estimate of the volume of polar cap material if lithospheric flexure is first ignored, we used the 1750-m surface contour, which approximates the edge of the polar layered deposits [unit Apl of (79)]. We then removed a trend surface, with a mean elevation of 1408 m, fit to the area outside this contour. The derived volume of cap material is  $1.5 \times 10^6 \text{ km}^3$ . Given its thickness and spatial extent, the southern layered terrain may constitute a significant lithospheric load, and thus assessment of the contribution due to lithospheric flexure of the layered deposits is required. We modeled the polar deposit load by a spherical harmonic expansion, to degree and order 90, of the south polar topography within the 1750-m contour. We considered elastic shell thickness values from 40 to 200 km. Because of the uncertainty in the density of the polar layered unit, we used load densities of  $1000 \text{ kg m}^{-3}$  (pure  $\text{H}_2\text{O}$  ice) and  $2000 \text{ kg m}^{-3}$  (ice plus dust). Forward models of loading of a spherical elastic shell (57, 52) by a load approximating the southern polar deposits indicate that the base of these deposits could extend from 300 to 2500 m beneath the cap edge, yielding additional contributions to the volume from  $4.0 \times 10^5$  to  $1.5 \times 10^6 \text{ km}^3$ . The total volume of cap material is thus 2 to  $3 \times 10^6 \text{ km}^3$ . The south polar volume has recently been estimated from stereo imaging to be  $1.6 \times 10^6$  to  $2.3 \times 10^6 \text{ km}^3$  (49). The MOLA topographic surface is about two orders of magnitude more precise than that from the images, and in addition, individual elevations from MOLA are geodetically referenced and permit the topography of the cap to be related accurately to the surroundings. The stereo-based estimate did not consider the effect of flexure of the basal surface, which is responsible for the bulk of the uncertainty in our estimate of the south polar volume, and which may contribute as much as half of the volume. Error due to the presence of the Prometheus Rupes under part of the layered terrain is small in comparison to the uncertainty associated with flexure.
54. D. A. Paige and K. D. Keegan, *J. Geophys. Res.* **99**, 25993 (1994).
55. M. T. Zuber, L. Lim, H. J. Zwally, in *First International Conference on Mars Polar Science and Exploration*, Camp Allen, TX, 18 to 22 October 1998; S. Clifford, D. Fisher, J. Rice, Eds. (Lunar Planetary Institute, Houston, 1998), pp. 45–46; W. B. Durham, *ibid.*, pp. 8–9.
56. M. H. Carr, *Water on Mars* (Oxford Univ. Press, New York, 1996).
57. S. M. Clifford, *J. Geophys. Res.* **92**, 9135 (1987); *ibid.* **98**, 10973 (1993).
58. T. J. Parker *et al.*, *Icarus* **82**, 111 (1989); T. J. Parker, D. S. Gorsline, R. S. Saunders, D. C. Pieri, D. M. Schneeberger, *J. Geophys. Res.* **98**, 11061 (1993); V. R. Baker *et al.*, *Nature* **352**, 589 (1991).
59. M. H. Carr and G. D. Clow, *Icarus* **48**, 91 (1981).
60. M. C. Malin and M. H. Carr, *Nature* **397**, 589 (1999).
61. B. K. Luchitta *et al.*, in (24), pp. 453–492.
62. U.S.G.S., *U.S. Geol. Surv. Misc. Inv. Series Map I-1712* (1986).
63. F. G. Lemoine *et al.*, "Precision orbit determination for Mars Global Surveyor during Hiatus and SPO," *IAAA Space Flight Mechanics Meeting*, Breckenridge, CO, 7 to 10 February 1999; (American Astronautics Society Publications Office, San Diego, 1999).
64. G. A. Neumann and D. W. Forsyth, *Mar. Geophys. Res.* **17**, 221 (1995).
65. The mean radius was obtained from a 36th degree and order spherical harmonic expansion of the binned data. The uncertainty is based on the rms fit of 554 m of the model to the data. The north and south polar radii are also determined from the harmonic model.

66. The mean equatorial radius was derived from the harmonic model (65) based on a 1° sampling of an equatorial profile. This value is 200 m larger than was estimated from earlier data (5) but is within the error estimate of the earlier value. The uncertainty corresponds to the standard error of the mean of the 360 equatorial samples.
67. We acknowledge the MOLA instrument team and the MGS spacecraft and operation teams at the Jet Propulsion Laboratory and Lockheed-Martin Astronau-

tics for providing the engineering foundation that enabled this analysis. We also thank G. Elman, P. Jester, and J. Schott for assistance in altimetry processing, D. Rowlands and S. Fricke for help with orbit determination, S. Zhong for assistance with the Helix relaxation calculation, and G. McGill for a constructive review. The MOLA investigation is supported by the NASA Mars Global Surveyor Project.

21 April 1999; accepted 10 May 1999

such a young age by such a wide array of recent independent measurements.

**Method**

Any measurement of a function of  $h$ ,  $\Omega_m$ , and  $\Omega_\Lambda$  can be included in a joint likelihood

$$L(h, \Omega_m, \Omega_\Lambda) = \prod_{i=1}^N L_i \tag{1}$$

which I take as the product of seven of the most recent independent cosmological constraints (Table 1 and Fig. 3). For example, one of the  $L_i$  in Eq. 1 represents the constraints on  $h$ . Recent measurements can be summarized as  $\bar{h} = 0.68 \pm 0.10$  (16). I represent these measurements in Eq. 1 by the likelihood

$$L_{\text{Hubble}}(h) = \exp \left[ -0.5 \left( \frac{h - \bar{h}}{0.10} \right)^2 \right] \tag{2}$$

Another  $L_i$  in Eq. 1 comes from measurements of the fraction of normal baryonic matter in clusters of galaxies (14) and estimates of the density of normal baryonic matter in the universe [ $\Omega_b h^2 = 0.015 \pm 0.005$  (15, 18)]. When combined, these measurements yield  $\bar{\Omega}_m h^{2/3} = 0.19 \pm 0.12$  (19), which contributes to the likelihood through

$$L_{\text{baryons}}(h, \Omega_m) = \exp \left[ -0.5 \left( \frac{\Omega_m h^{2/3} - \bar{\Omega}_m h^{2/3}}{0.12} \right)^2 \right] \tag{3}$$

The ( $\Omega_m, \Omega_\Lambda$ )-dependencies of the remaining five constraints are plotted in Fig. 3 (20). The 68% confidence level regions derived from CMB and SNe (Fig. 3, A and B) are nearly orthogonal, and the region of overlap is relatively small. Similar complementarity exists between the CMB and the other data sets (Fig. 3, C through E). The combination of them all (Fig. 3F) yields  $\Omega_\Lambda = 0.65 \pm 0.13$  and  $\Omega_m = 0.23 \pm 0.08$  (21).

This complementarity is even more important (but more difficult to visualize) in three-dimensional parameter space, ( $h, \Omega_m, \Omega_\Lambda$ ). Although the CMB alone cannot tightly constrain any of these parameters, it does have a strong preference in the three-dimensional space ( $h, \Omega_m, \Omega_\Lambda$ ). In Eq. 1, I used  $L_{\text{CMB}}(h, \Omega_m, \Omega_\Lambda)$ , which is a generalization

# A Younger Age for the Universe

Charles H. Lineweaver

The age of the universe in the Big Bang model can be calculated from three parameters: Hubble’s constant,  $h$ ; the mass density of the universe,  $\Omega_m$ ; and the cosmological constant,  $\Omega_\Lambda$ . Recent observations of the cosmic microwave background and six other cosmological measurements reduce the uncertainty in these three parameters, yielding an age for the universe of  $13.4 \pm 1.6$  billion years, which is a billion years younger than other recent age estimates. A different standard Big Bang model, which includes cold dark matter with a cosmological constant, provides a consistent and absolutely time-calibrated evolutionary sequence for the universe.

In the Big Bang model, the age of the universe,  $t_o$ , is a function of three parameters:  $h$ ,  $\Omega_m$ , and  $\Omega_\Lambda$  (1). The dimensionless Hubble constant,  $h$ , tells us how fast the universe is expanding. The density of matter in the universe,  $\Omega_m$ , slows the expansion, and the cosmological constant,  $\Omega_\Lambda$ , speeds up the expansion (Fig. 1).

Until recently, large uncertainties in the measurements of  $h$ ,  $\Omega_m$ , and  $\Omega_\Lambda$  made efforts to determine  $t_o$  ( $h, \Omega_m, \Omega_\Lambda$ ) unreliable. Theoretical preferences were, and still are, often used to remedy these observational uncertainties. One assumed the standard model ( $\Omega_m = 1, \Omega_\Lambda = 0$ ), dating the age of the universe to  $t_o = 6.52/h$  billion years old (Ga). However, for large or even moderate  $h$  estimates ( $\geq 0.65$ ), these simplifying assumptions resulted in an age crisis in which the universe was younger than our Galaxy ( $t_o \approx 10$  Ga  $<$   $t_{\text{Gal}} \approx 12$  Ga). These assumptions also resulted in a baryon crisis in which estimates of the amount of normal (baryonic) matter in the universe were in conflict (2, 3).

Evidence in favor of  $\Omega_m < 1$  has become more compelling (4–8), but  $\Omega_\Lambda$  is still often assumed to be zero, not because it is measured to be so, but because models are simpler without it. Recent evidence from supernovae (SNe) (4, 5) indicates that  $\Omega_\Lambda > 0$ . These SNe data and other data exclude the standard Einstein-deSitter model ( $\Omega_m = 1, \Omega_\Lambda = 0$ ). The cosmic microwave background (CMB), on the other hand, excludes models with low  $\Omega_m$  and  $\Omega_\Lambda = 0$  (3). With both high and low  $\Omega_m$  excluded,  $\Omega_\Lambda$  cannot be zero. Combining CMB measure-

ments with SNe and other data, I (9) have reported  $\Omega_\Lambda = 0.62 \pm 0.16$  [see (10–12) for similar results]. If  $\Omega_\Lambda \neq 0$ , then estimates of the age of the universe in Big Bang models must include  $\Omega_\Lambda$ . Thus, one must use the most general form:  $t_o = f(\Omega_m, \Omega_\Lambda)/h$  (13).

Here, I have combined recent independent measurements of CMB anisotropies (9), type Ia SNe (4, 5), cluster mass-to-light ratios (6), cluster abundance evolution (7), cluster baryonic fractions (14), deuterium-to-hydrogen ratios in quasar spectra (15), double-lobed radio sources (8), and the Hubble constant (16) to determine the age of the universe. The big picture from the analysis done here is as follows (Figs. 1 and 2): The Big Bang occurred at  $\sim 13.4$  Ga. About 1.2 billion years (Gy) later, the halo of our Galaxy (and presumably the halo of other galaxies) formed. About 3.5 Gy later, the disk of our Galaxy (and presumably the disks of other spiral galaxies) formed. This picture agrees with what we know about galaxy formation. Even the recent indications of the existence of old galaxies at high redshift (17) fit into the time framework determined here. In this sense, the result is not surprising. What is new is the support given to

**Table 1.** Parameter estimates from non-CMB measurements. I refer to these as constraints. I use the error bars cited here as  $1\sigma$  errors in the likelihood analysis. The first four constraints are plotted in Fig. 3, B through E.

Method	Reference	Estimate
SNe	(35)	$\Omega_m^{\Lambda=0} = -0.28 \pm 0.16, \Omega_m^{\text{flat}} = 0.27 \pm 0.14$
Cluster mass-to-light	(6)	$\Omega_m^{\Lambda=0} = 0.19 \pm 0.14$
Cluster abundance evolution	(7)	$\Omega_m^{\Lambda=0} = 0.17^{+0.28}_{-0.10}, \Omega_m^{\text{flat}} = 0.22^{+0.25}_{-0.10}$
Double radio sources	(8)	$\Omega_m^{\Lambda=0} = -0.25^{+0.70}_{-0.50}, \Omega_m^{\text{flat}} = 0.1^{+0.50}_{-0.20}$
Baryons	(19)	$\Omega_m h^{2/3} = 0.19 \pm 0.12$
Hubble	(16)	$h = 0.68 \pm 0.10$

School of Physics, University of New South Wales, Sydney NSW 2052, Australia. E-mail: charley@bat.phys.unsw.edu.au